Reviewed research article

The May 29th 2008 earthquake aftershock sequence within the South Iceland Seismic Zone: Fault locations and source parameters of aftershocks

Bryndís Brandsdóttir[1], Matthew Parsons[2], Robert S. White[2], Ólafur Guðmundsson[1,3,4], Julian Drew[2] and Bergþóra S. Thorbjarnardóttir[5]

[1]*Institute of Earth Sciences, Science Institute, University of Iceland*

[2]*Department of Earth Sciences, Bullard Laboratories, University of Cambridge, England, UK*

[3]*Department of Science and Engineering, Reykjavík University, Iceland*

[4]*Department of Earth Sciences, Uppsala University, Villavägen 16, SE-752 36 Uppsala, Sweden*

[5]*Icelandic Meteorological Office, Reykjavík, Iceland*

bryndis@raunvis.hi.is, mdp31@cam.ac.uk, rsw1@esc.cam.ac.uk, ogud@ru.is, drew2@slb.com, begga@vedur.is

Abstract — *On May 29th 2008, two M_w ∼6 earthquakes struck the western part of the South Iceland Seismic Zone. The first event was followed within seconds by a similar size event on a second fault ∼5 km further west. Earthquakes, detected by a temporary network of 11 seismometers and three permanent SIL-network stations were located using an automated Coalescence Microseismic Mapping technique. The epicenters delineate two major and several smaller N-S faults as well as an E-W zone of activity stretching further west into the Reykjanes Peninsula Rift Zone. Fault plane solutions show right lateral strike slip mechanisms along the two major N-S faults and suggest both smaller N-S right-lateral strike slip faults further west as well as an E-W zone of left lateral strike slip fault. The aftershocks deepen from 3–5 km in the north to 8–9 km in the south, suggesting that the main faults dip southwards. A brief increase in aftershock seismicity is most likely caused by short-term static stress buildup on adjacent faults. The faulting is interpreted to be driven by the local stress due to transform motion between two parallel segments of the divergent plate boundary crossing Iceland.*

INTRODUCTION

The mid-Atlantic plate boundary breaks up into a series of segments across Iceland (Figure1). The South Iceland Seismic Zone (SISZ) is a complex transform zone where left-lateral E-W shear between the Reykjanes Peninsula Rift Zone and the Eastern Volcanic Zone is accommodated by bookshelf faulting along N-S lateral strike-slip faults (Einarsson *et al.*, 1981). The SISZ is also a transient feature, migrating laterally in response to the southward propagation of the Eastern Volcanic Zone. Sequences of large earthquakes (M > 6) lasting from days to years and affecting most of the seismic zone have occurred repeatedly in historical time (last 1100 years), separated by intervals of relative quiescence lasting 45–112 years (Einarsson and Björnsson, 1979). The latest earthquake sequences occurred in 1896, 1912, 1987 and 2000. They typically start with a large earthquake in the eastern part of the SISZ followed by events of equal or smaller magnitude further west. A major sequence activating faults through the whole SISZ region occurred in 1896 with five M_s 6–6.9 events taking place over a period of two weeks (Einarsson *et*

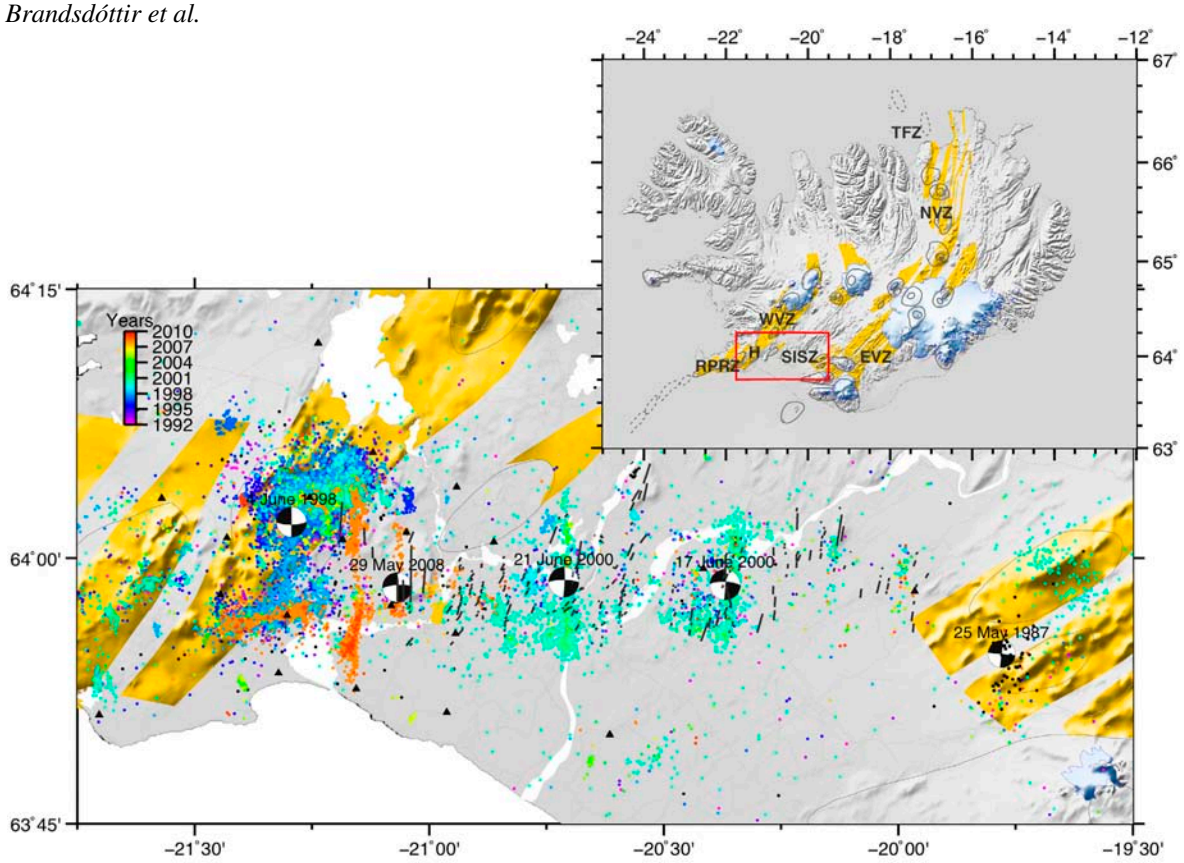

Figure 1. Seismicity within the South Iceland Seismic Zone and Hengill Triple Junction (H), 1992–2009. Event locations from the IMO published in the SIL database (2009) are color coded by time. Surface strike-slip faults mapped by Einarsson (this issue) are shown with dark grey lines. Fault plane solutions for historical mainshocks are from the CMT Catalogue (2009). Fault plane solution, fore- and aftershocks (black) of the 1987 Vatnafjöll earthquake are from Bjarnason and Einarsson (1991). Temporary seismic stations have black triangles and permanent stations red. Roads are light grey. Upper right: A structural map of the plate boundary of Iceland (Einarsson and Saemundsson, 1987). A red square marks the study area within the South Iceland Seismic Zone (SISZ). Fissure swarms of individual volcanic systems within the volcanic zones are yellow. Reykjanes Peninsula Rift Zone (RPRZ), Western Volcanic Zone (WVZ), Eastern Volcanic Zone (EVZ), Northern Volcanic Zone (NVZ) and the Tjörnes Fracture Zone (TFZ). – *Upptök jarðskjálfta í brotabelti Suðurlands og á Hengilssvæðinu, 1992–2009, samkvæmt gögnum úr SIL-gagnagrunni Veðurstofu Íslands og gagnagrunni Raunvísindastofnunar Háskólans frá 1987. Brotlausnir stærstu skjálftanna eru frá Harvard CMT listanum og grein I. Bjarnasonar og P. Einarssonar (1991). Dökkgráar línur sýna legu jarðskjálftasprungna á yfirborði, sjá grein Páls Einarssonar í þessu hefti. Þríhyrningar tákna jarðskjálftamælistöðvar, rauðir (SIL) og svartir (Loki). Brotlausnir stærstu skjálftanna og eftirskjálftavirkni gefa til kynna hægri-handar sniðgengi á N-S lægum misgengjum.*

al., 1981). A new sequence seems to be in progress, initiated by a M_s 5.8 earthquake by Vatnafjöll, on the western flank of the EVZ and two M_w 6.5 (NEIC) earthquakes in the eastern part of the SISZ on June 17 and 21, 2000. These events were followed by two earthquakes with moment magnitudes of M_w 5.8 and M_w 5.9 within the western SISZ on May 29th 2008 (Decriem *et al.*, 2010). The mainshock magnitude is M_w 6.3 based on teleseismic data (Harvard).

A dense network of seismographs encompassing the earthquake source region lowers detection thresholds and reduce location uncertainty. Following the May 29th 2008 events, a temporary network of eleven seismometers (Figure 1) was deployed within the region in order to obtain accurate aftershock locations for 3-D imaging of active faults. This LOKI network located thousands of aftershocks during the following days, delineating two major and several smaller faults. We applied a coalescence microseismic mapping method (CMM) for detection and localization of the aftershock sequence of the two May 29, 2008 Ölfus earthquakes. The technique is both automatic and robust. The algorithm performs an exhaustive search in time and space for events, and incorporates traveltime inverse theory in imaging earthquake locations (Drew *et al.*, 2005; Drew, 2010).

Tectonics of the South Iceland Seismic Zone

The SISZ is markedly different from fracture zones elsewhere along the Mid-Atlantic Ridge plate boundary with minimal surface relief and diffuse tectonics. Seismic and geodetic data show the over-all left-lateral transform motion within the SISZ to be accommodated by bookshelf faulting along N-S aligned, right-lateral, strike-slip faults (Einarsson *et al.*, 1981; Hackman *et al.*, 1990; Einarsson, 1991; Rognvaldsson and Slunga, 1994; Sigmundsson *et al.*, 1995; Hreinsdóttir *et al.*, 2001, 2009; Dubois *et al.*, 2008). Detailed surface mapping shows the SISZ to be made up of more than twenty N-N20E oriented, en echelon strike-slip faults (Einarsson and Eiríksson, 1982; Bjarnason *et al.*, 1993; Bergerat and Angelier, 2003; Clifton and Einarsson, 2005) which extend westwards across the Reykjanes Peninsula Rift Zone (Sæmundsson and Einarsson, 1980; Sæmundsson 1995; Clifton and Kattenhorn, 2006).

The SISZ, from the Hengill Triple Junction in the west, to the Eastern Volcanic Zone, is represented by a roughly 10 km wide band of seismicity (Einarsson, 1991; Stefánsson, 1993; Bjarnason *et al.*, 1993). Aftershocks of the M_s 5.8 1987 Vatnafjöll earthquake define a 12 km long and 4 km wide zone, between 6 and 13 km depth (Bjarnason and Einarsson, 1991), whereas aftershocks of the two M_w 6.5 earthquakes in 2000 delineate approximately 12.5 km and 16.5 long zones down to 10 km depth (Hjaltadóttir and Vogfjörð, 2005). Geodetic modelling based on joint inversion of InSAR and GPS measurements indicates two 15 km long, near vertical faults extending from the surface to approximately 10 km depth (Pedersen *et al.*, 2003), in good agreement with the aftershock distribution. The Vatnafjöll earthquake rupture did not reach the surface.

The long term average spreading direction across Southern Iceland, $\sim$103° (NUVEL-1A, DeMets *et al.*, 1994), was shown by early modelling of GPS measurements to cause accumulation of left-lateral shear strain across a 20–30 km wide (N-S) zone (e.g. Sigmundsson *et al.*, 1995). More recent models show the SISZ as a complex zone driven by N-S faulting near the surface and E-W left-lateral shear below 15–20 km depth (Árnadóttir *et al.*, 2006). Mapped surface faults range in length from less than 1 km at the westernmost tip of the RPRZ to 10–15 km near the centers of the RPRZ and SISZ (Clifton and Einarsson, 2005; Clifton and Kattenhorn, 2006).

Aftershocks from the 2008 earthquakes delineate two parallel N-S trending, segmented faults 4–5 km apart, with additional activity stretching westward along an E-W aligned zone (Figure 1). Models of geodetic observations (GPS and InSAR) yield a total moment release of M_w 5.8 for the first event and M_w 5.9 for the second event, with a composite moment of M_w 6.1 for both events (Decriem *et al.*, 2010) in right-lateral strike-slip motion on two parallel N-S trending faults. Only minor slip was observed on other structures illuminated by earthquake activity. High rate (1 Hz) continuous GPS data also indicate that the western fault event occurred within 3 s of the main event on the eastern fault (Hreinsdóttir *et al.*, 2009, Decriem *et al.*, 2010).

DATA ACQUISITION

Within two days of the May 29th events, 11 portable seismometers were deployed around the two faults that had ruptured, to augment earthquake locations by the permanent network. The LOKI network was operated until July 2nd and recorded over twenty thousand events.

The primary aim of this project was to delineate the complicated fault network based on detailed aftershock locations and determine focal mechanisms of the bigger aftershocks in order to constrain the rupture geometry along both faults within the context of the SISZ. An automated picking program was used for earthquake locations which were compared with the Icelandic Meteorological Office (IMO) SIL catalog locations. We used data from the eleven temporary stations (Table 1) and three SIL stations, BJA, KRO and SOL. The online SIL catalogue was used to determine event magnitudes (Figure 2) as the CMM program does not calculate magnitudes. The SIL provides local moment magnitudes, M_{lw} (Jakobsdóttir, 2008). Earthquakes larger than 4 may be severely underestimated by the M_{lw} scale.

About a week after being deployed station HOLL was run over by a bulldozer working on a neighbouring road. This resulted in a data gap for about 24 hours until station INGO was rebuilt nearby. The broadband station UGAR, deployed June 21st was omitted due to a faulty sensor.

Coalescence Microseismic Mapping (CMM)

The CMM technique of Drew (2010) is an automated earthquake location process. CMM is a numerical imaging technique while at the same time an event location algorithm with a theoretical basis in the Bayesian inversion of arrival times (Tarantola and Valette, 1982). Rather than reducing the data to discrete arrival time picks, the CMM method continuously maps a short/long time (STA/LTA) average signal for each phase for each station. The resultant spatio-temporal maps identify likely times and locations of events, as points of coalescence of the mapped signals (Figures 3 and 4). In as far as the STA/LTA signal relates to the statistical variability of time picks, where the time picks are taken as the local maxima of the STA/LTA function, the objective function is the

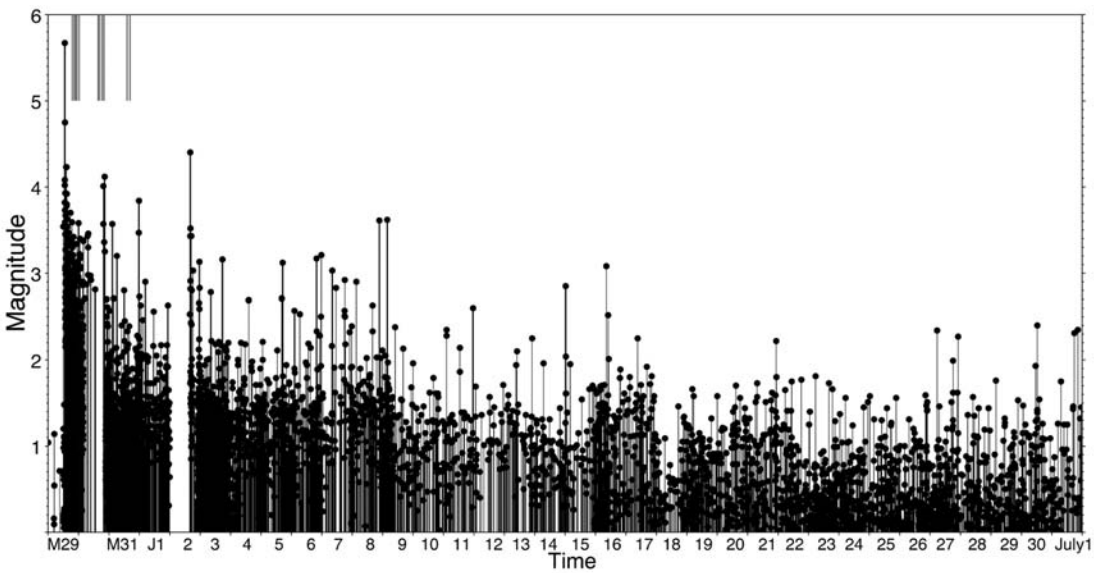

Figure 2. Local moment magnitudes M_{lw} of SIL located events May 29th to July 1st, Julian days 150 to 183. A total of 5737 events. The mainshock moment magnitude M_w 6.3 derived from teleseismic data (CMT-Harvard) is underestimated by the local network. Grey bars mark deployment of temporary stations. Manual review of the automatic locations is incomplete for May 30th and June 2nd. – *Stærðardreifing eftirskjálfta. Gögn úr SIL-gagnagrunni Veðurstofu Íslands. Hluti gagnanna er óunninn. Stærsti skjálftinn er vanmetinn á nálægari stöðvum, hann mældist M_w 6.3 stig á erlendum mælistöðvum. Gráar línur tákna uppsetningartíma færanlegra jarðskjálftamæla, sbr. töflu 1.*

posterior probability for the time and location of an event. This has been verified experimentally (Drew *et al.*, 2005; Drew, 2010). For this data, an STA/LTA ratio of 0.1/ 0.4 s was used to detect P phases and 0.2/0.6 s to detect S_H phases.

Table 1. LOKI stations deployment overview. – *Uppsetning færanlegra jarðskjálftamæla.*

Station Name	Deployment		Station code
GUFU	29/5/2008	21:46	9881
SOLV	29/5/2008	23:16	987A
ORLH	30/5/2008	00:30	988B
HEIDI	30/5/2008	01:13	9870
HOLL	30/5/2008	03:10	987B
RAUH	30/5/2008	18:00	9886
RANI	30/5/2008	19:00	9879
HOLT	30/5/2008	21:02	987C
HALS	30/5/2008	22:34	A01A
BURF	31/5/2008	16:53	A06F
VNES	31/5/2008	19:02	A06E
UGAR	21/6/2008	16:31	986F

The program exists in two forms, CMM Detect and CMM Locate. Both programs make use of a Look Up Table (LUT) of modelled travel times from each station to every cell of a specified grid (i.e. a search area). CMM Detect performs a systematic exhaustive search over the grid, with candidate events identified as the time and location that the coalescence function exceeds a pre-set threshold (Figure 3). CMM Locate takes a list of event times, and evaluates the objective function over short time windows, returning an updated estimate of the time and location for each event. This is much quicker and easier than re-running CMM Detect, allowing the effects of changes to input parameters to be quickly tested.

A cell size of 320 m^3 was used for most of the runs, then reduced to 230 m^3 for the final run of CMM Locate. Using smaller cells is computationally more costly, without necessarily resulting in any real gains in accuracy. The optimal spatial sampling is governed by the shape (smoothness) of the mapped objective function, which is in turn governed by the input data (the constraints on arrival times) and the misfit between data and model (residual).

The time corresponding to the local maximum of the STA/LTA signal, will be shifted in time with respect to an interactive arrival time pick. As long as the shift in time is consistent between the time picks for each of the phase arrivals, the result is a shift in the estimated time of the event, not the estimated location. As the CMM program exhaustively evaluates for all times, it will also evaluate a second peak of emergent P energy arrivals. However, as long as the signal-to-noise ratio of the primary arrival is bigger, and the primary arrival fits the modelled traveltime equally well, the CMM estimated time and location will correspond to the primary arrival.

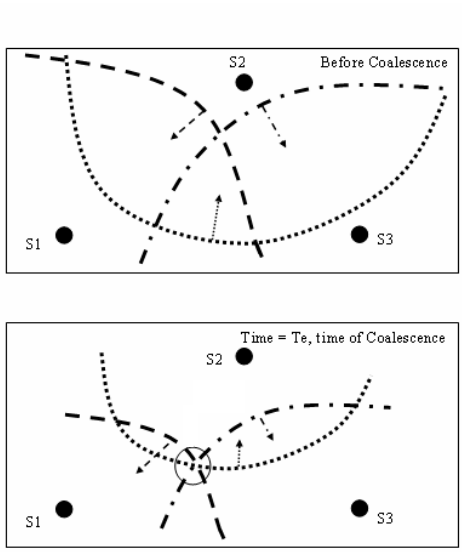

Figure 3. Cartoon showing coalescence of signals from three stations. The dashed lines mark equal ray travel time from each of the stations. As they are migrated back towards their respective stations, they eventually intersect at the event location. Figures from Drew (2010). – *CMM forritið skynjar og staðsetur jarðskjálfta með því að nema útslag og bera saman reiknaðan ferðatíma til hverrar stöðvar.*

Utilizing a cluster, with each day of data processed as a separate run, the time required to processes the dataset was between 24 and 36 hours. In each run the data was band-pass filtered 2–12 Hz for S waves and 4–20 Hz for P waves.

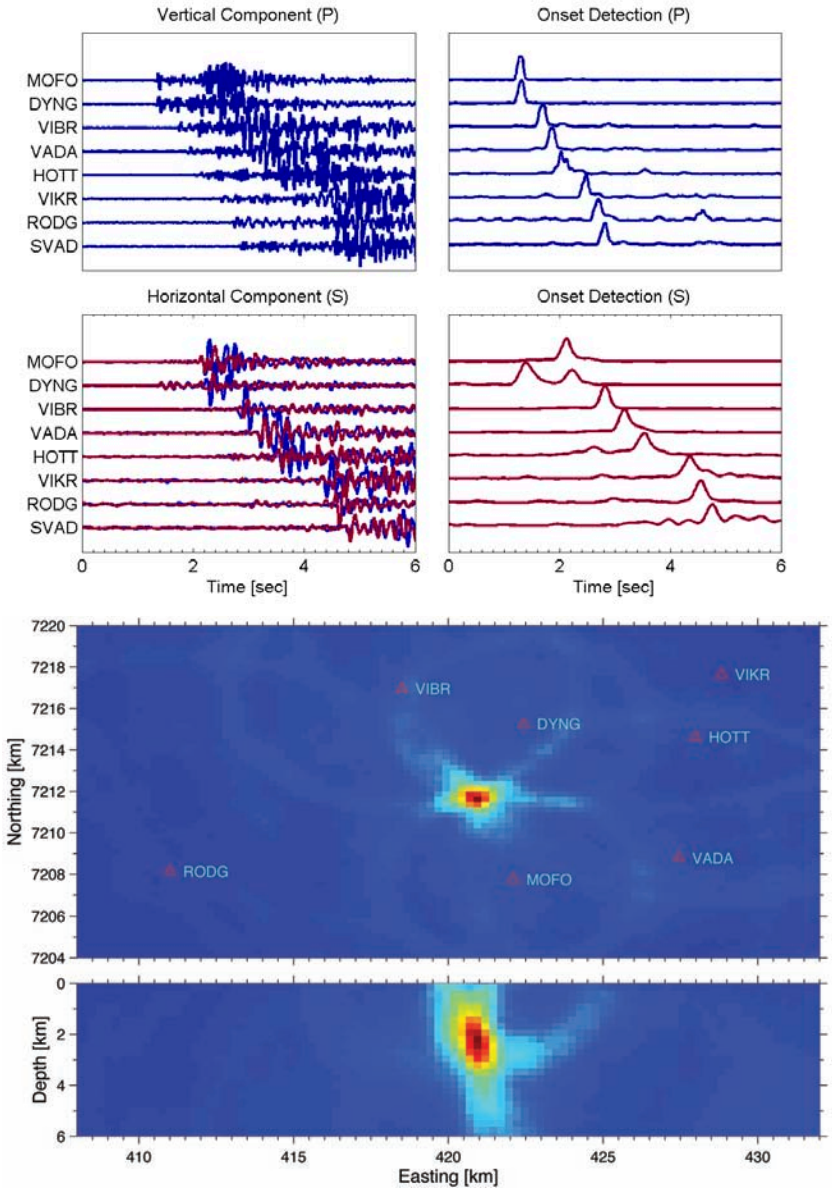

Figure 4. CMM search in time and space for events. Top: Onset arrival detection for the compressional and shear arrivals of an earthquake in Askja. Below: The CMM map of coalescence of signals from seven local stations. Lighter colored ellipses mark equal ray travel time from different stations which intersect at the red colored event location. From Drew (2010). – *CMM staðsetningarforritið nemur P- og S-bylgjur jarðskjálfta og reiknar staðsetningu (rautt svæði) út frá ferðatíma til jarðskjálftamælanna. Gögn frá stöðvum við Öskju.*

The LUT was calculated for a one-dimensional velocity model, being a simplification of the real three-dimensional crustal structure. Localised near surface velocity anomalies beneath each station could potentially have a considerable effect on their overall travel time. No station corrections were applied. The resultant location estimates and calculated uncertainties are impacted by the uncorrected delays. In addition to applying station correction terms, location errors could be further reduced by introducing source specific station terms (Richards-Dinger and Shearer, 2000) or using the double-difference relative location technique of Waldhauser and Ellsworth (2000).

EARTHQUAKE LOCATIONS

Three sets of data were run through the CMM programs, initially using only data from the 11 tempoary LOKI stations, followed by a rerun with additional three SIL stations and finally data from nine SIL stations. A total of $\sim$19450 events were located using data from 14 stations. Using the 11 LOKI stations CMM detected 11057 events. Smaller, poorly constrained events were omitted resulting in 13868 events with signal-to-noise (SN) ratio >2.5 and 7846 events with SN ratio >3 and epicentral and depth location errors within 1 km and 2 km, respectively. The significant jump in the number of detected events with 14 stations is due to more events being located during the first two days while the LOKI network was being installed as well as improved event detection. Running CMM with both the LOKI and SIL station data produced less scatter of events and better defined faults within the epicentral zone. Running CMM on data from nine SIL stations resulted in 18504 events being detected, of which 6824 passed filtering.

Most events have latitude and longitude errors 0.7 ± 0.3 km and depth errors 1 ± 0.5 km, as estimated by the CMM algorithm. These errors are within one standard deviation measure as determined by the computed probability density function (*pdf*). Each numerically computed event location *pdf* incorporates inherent assumptions regarding uncertainty, including the measurement uncertainty as governed by the choice of parameters for the STA/LTA function. As with other location algorithms that have their own inherent assumption, the uncertainty estimates provide a relative measure of confidence in the location estimates. In addition we assessed variations in crustal structure by running CMM on three different crustal models, see discussion below. No observed change in epicentral distribution was observed showing the CMM result to be quite robust against variations in velocity.

The epicentral map is dominated by seismicity along two parallel N–S trending faults spaced 4–5 km apart and diffuse activity stretching mainly westward along an E-W aligned zone (Figures 1 and 5), into an E-W zone mapped by Vogfjörd *et al.* (2005) from the aftershock activity of the 13 November 1998 earthquake. Considerably smaller aftershock activity is observed on the eastern N-S fault (Ingólfsfjall), possibly suggesting that the mainshock rupture left little residual stress on the fault to cause aftershocks. Given the extent of the aftershock clusters, they mark the fault as being about 13 km long. The second main fault (named Reykjafjall or Kross fault) lies about 5 km to the west and is slightly longer ($\sim$17 km). Most of the aftershock activity originated along this fault. Several smaller N-S faults are also active within the main E-W zone. Events outside the seismic network, at the western and eastern ends of the E-W zone, are not well constrained. Clustering of event locations suggests the main faults to be made up of numerous smaller segments branching into conjugate faults at each end (see discussion below). The two cross sections highlight the depth distribution of events. Most aftershocks lie between 1 and 9 km depth along the two main faults with the eastern fault having a slightly smaller depth distribution than the western fault, whereas events along the E-W zone west of the main faults are concentrated below 5 km depth. Hypocentral depths are markedly shallower along the northern portion of both major fault where they extend down to 4–6 km, deepening southwards to 9 km. Of note is the relative lack of events in the middle of the fault, where the two main events originated (Hreinsdóttir *et al.*, 2009).

A more direct comparison of the CMM and SIL locations along the two major N-S faults underlines how a dense local network around the epicentral zone is required in order to constrain the depth distribution

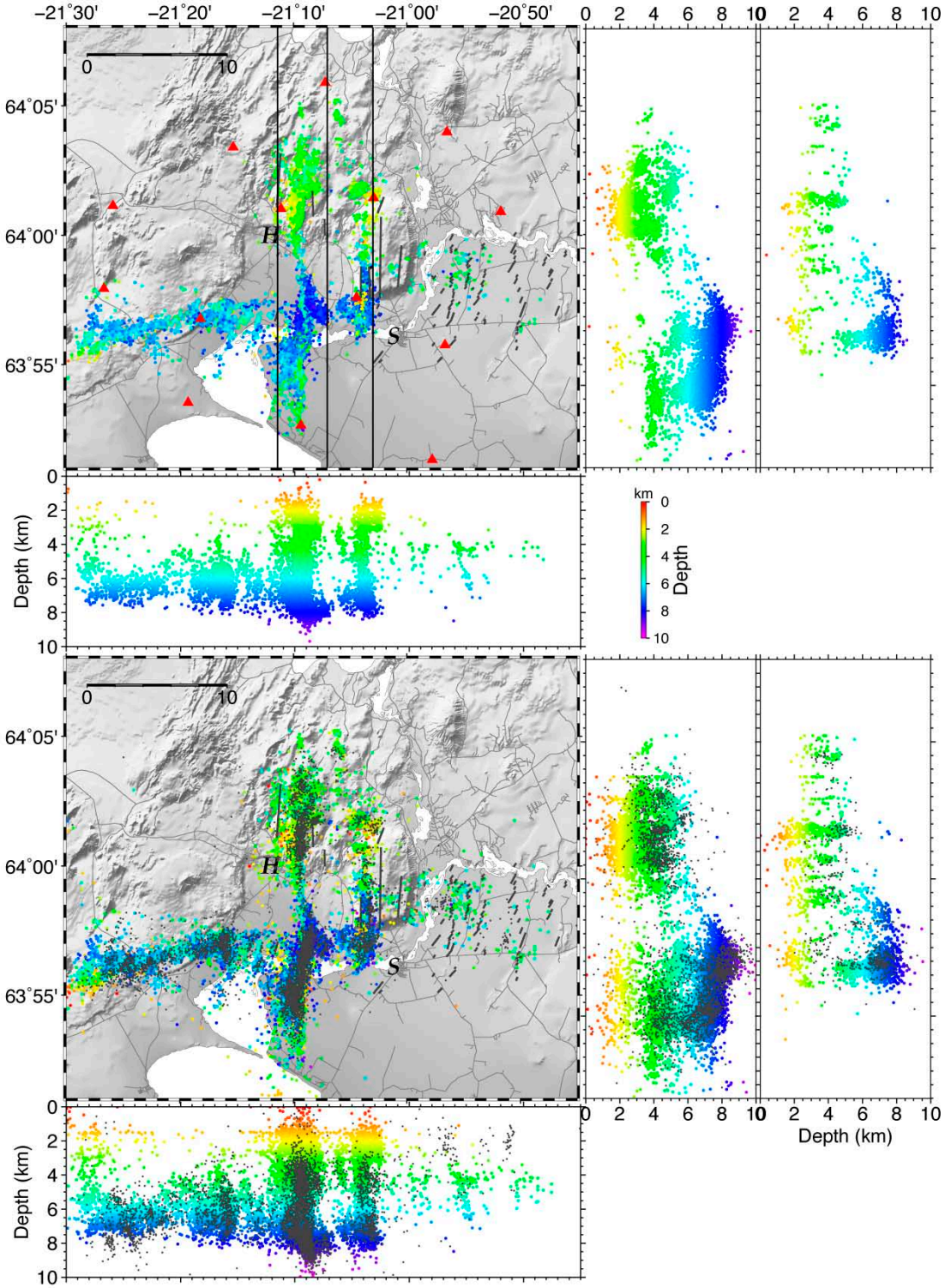
−21°30'
−21°20'
−21°10'
−21°00'
−20°50'
0
10
64°05'
64°00'
63°55'
H
S
Depth (km)
km
Depth
0
2
4
6
8
10

of the smaller events. Although the SIL–catalogue is missing some data May 30th and June 2nd (Figure 2), the overall distribution correlates well with the CMM locations (Figure 6a-c). Using only SIL data, the CMM program has difficulties constraining hypocentral depths, with many events at a default depth of 1.5 km. Given that there are only three SIL stations within the epicentral region and CMM was never designed to work with far-field stations, it is not surprising that it has not been very successful. The fact that it has produced a similar planar view is encouraging.

The SIL located events lie systematically about 500 m east of the CMM locations in the northern epicentral zone (Figure 7) where hypocenters are shallower. Shallower events (above 4 km) are also systematically located deeper by SIL than by CMM (Figure 6). Both SIL and CMM locations are based on a 1-D velocity model derived from the SIST refraction profile for the SISZ (Bjarnason *et al.*, 1991). In order to test how slight regional variations in upper crustal velocities may affect CMM locations we relocated all events using the 1-D model SUL (Figure 8) derived by Vogfjörd *et al.* (2002) for the Hengill-Hellisheiði region and a 1-D model derived from the RISE refraction profile which crosses the epicentral region (Weir *et al.*, 2001). The three models are very similar although the SUL and RISE models have slightly higher velocities between 3–6 km depth. In addition, the SUL model has a lower crustal velocity gradient below 6 km depth. Our results showed no marked shift in the epicentral zone between the SIL and SUL models (Figure 7, bottom). Locations of about 900 events on June 2 using the RISE model was identical to the other two models. Slightly higher velocities at 3–6 km depth may be responsible for deepening the SIL locations with respect to CMM locations. No station corrections were derived but localized near surface velocity anomalies could also potentially cause some of the observed shift in the epicentral zone for the shallower events as the SIL stations are distributed over a larger area than the 14 stations used for the CMM locations. A 500 m westward shift of the epicentral zone also fits GPS and InSAR coseismic deformation models for the Ingólfsfjall fault (Decriem *et al.*, 2010).

Fault Plane Solutions

Fault Plane Solutions were produced for 123 events spread over the epicentral area (Figures 9 and 10) using the program of Reasenberg and Oppenheimer (1985) which calculates best fit double-couple fault plane solutions from the polarity data. P and T axes were extracted using a modified version of FPPLOT and plotted using StereoNett (Duyster, 2000). The fault plane solutions were limited to events larger than M_{lw}1.3 and are thus generally well constrained, with strike, dip and rake uncertainties less than 15°, 25° and 20°, respectively. A total of 114 fault plane solutions had strike uncertainties of 8° or less.

The fault plane solution of the first event, from the Global CMT Harvard Catalogue (2009), is consistent with a right lateral strike slip fault on a N-S plane (Figure 10, lower right). Our fault plane solutions are also dominated by NNW-NE aligned strike slip faulting on individual fault strands with variable normal

Figure 5. Top: CMM located aftershocks (7846 events) with SN ratio greater than 3 and calculated epicentral and depth location errors less than 1 km and less than 2 km, respectively, using 14 LOKI and SIL stations (red triangles). The events are colored depending on depth. Flanking the epicentral map are two N-S transects along the main N-S faults (within the region marked by vertical lines) and an E-W transect across the whole zone. Events at the western end of the EW zone are not well constrained. The western fault borders the village of Hveragerði (H) and the town of Selfoss (S) lies 3 km east of the eastern fault. Below: for comparison, a total of 13868 CMM located aftershocks with SN ratio greater than 2.5. Also shown are 5189 SIL located events May 29–July 2 (grey dots) with epicentral and depth errors less than 1 km and 2 km. Roads are light grey and surface faults are dark grey. – *Upptakadreifing 7846 jarðskjálfta sem staðsettir voru með neti ellefu færanlegra mæla ásamt þremur SIL stöðvum (rauðir þríhyrningar). Jarðskjálftarnir eru litaðir eftir upptakadýpi. Reiknuð staðsetningaróvissa er innan við 1 km í láréttu plani og 2 km í dýpi. Til hægri eru þversnið af sprungunum við Reykjafjall, rétt austan Hveragerðis og Ingólfsfjall en fyrir neðan er þversnið yfir allt svæðið. Neðri myndin sýnir upptakadreifingu allra CMM staðsettra skjálfta, samtals 13868. Til samanburðar eru SIL staðsetningar á 5189 skjálftum (dökkgráir punktar).*

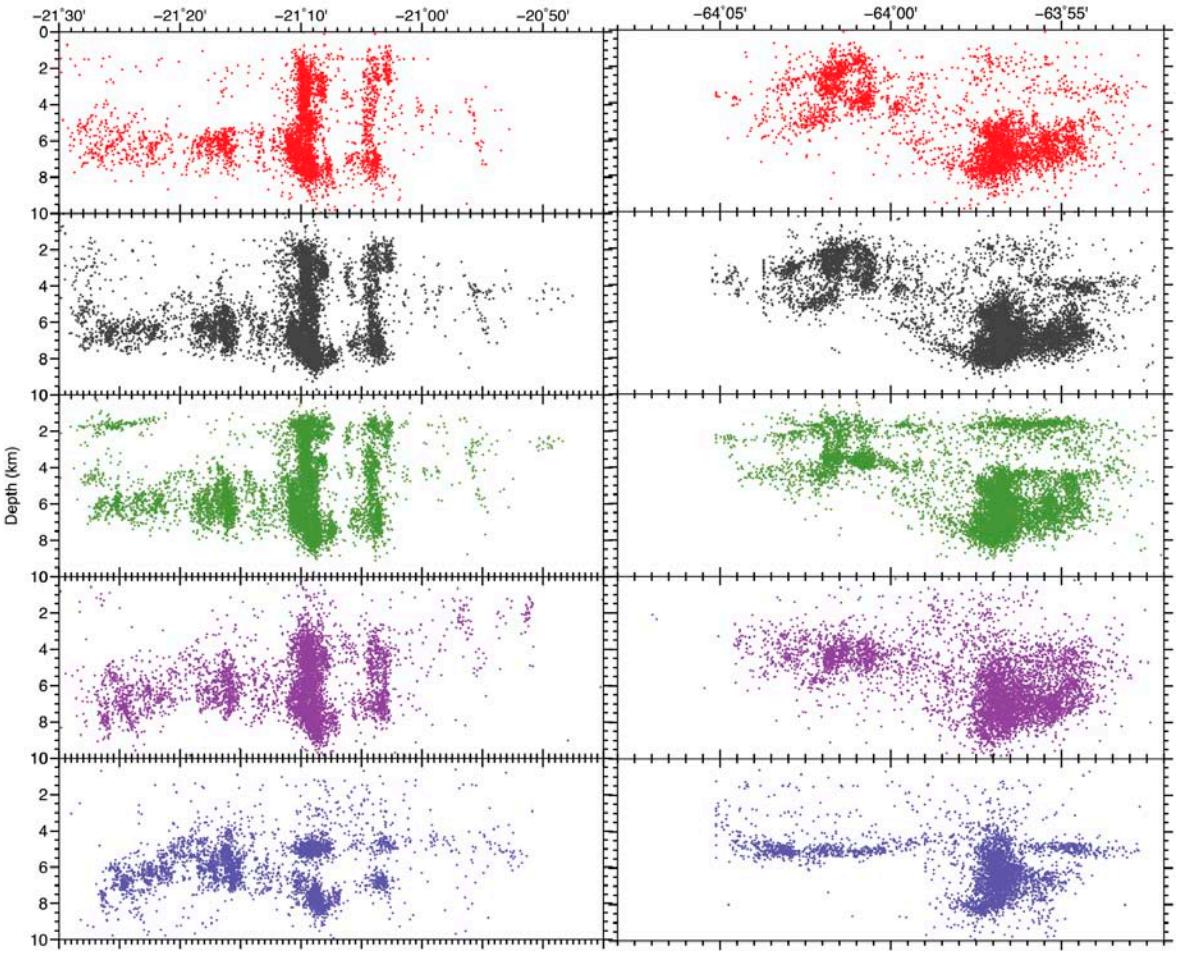

Figure 6. An overview of CMM and SIL located aftershocks, on W-E (left, looking north) and N-S (right, looking east) cross sections with location errors less than 2 km and SN ratio greater than 3. CMM locations with eleven LOKI stations and the SIL model (Figures 7 and 8) are red, a total of 4527 events. CMM locations of 8203 events, using eleven LOKI and three SIL stations and the SIL model are black. CMM locations of 8800 events, using 14 stations and the SUL model are green. SIL database locations with GAP <180, a total of 5737 events are purple and CMM locations using nine SIL stations, a total of 3982 events are violet. A horizontal or vertical line of events is an artefact from the CMM location process as these events did not have sufficient stations to be properly located. – *Samanburður á dýptardreifingu SIL og CMM staðsettra skjálfta með staðsetningaróvissu innan við 2 km. Efst eru CMM staðsetningar (rauðar) með ellefu færanlegum (Loka) mælum, 4527 skjálftar. CMM staðsetningar með SIL líkaninu á 8203 skjálftum með 14 stöðvum eru svartar. CMM staðsetningar á 8800 skjálftum með 14 stöðvum og SUL líkaninu eru grænar. SIL staðsetningar eru lillablåar, 5737 skjálftar. Neðst eru CMM staðsetningar með níu SIL stöðvum, 3982 skjálftar. Skjálftar vestast á svæðinu sem liggja rétt utan við mælanetið eru illa skorðaðir í dýpi. Enginn sjáanlegur munur er á CMM staðsetningum með mismunandi hraðalíkönum. CMM forritið á erfiðara með dýptarstaðsetningar SIL-gagna þar sem einungis þrjár SIL stöðvar eru innan upptakasvæðisins.*

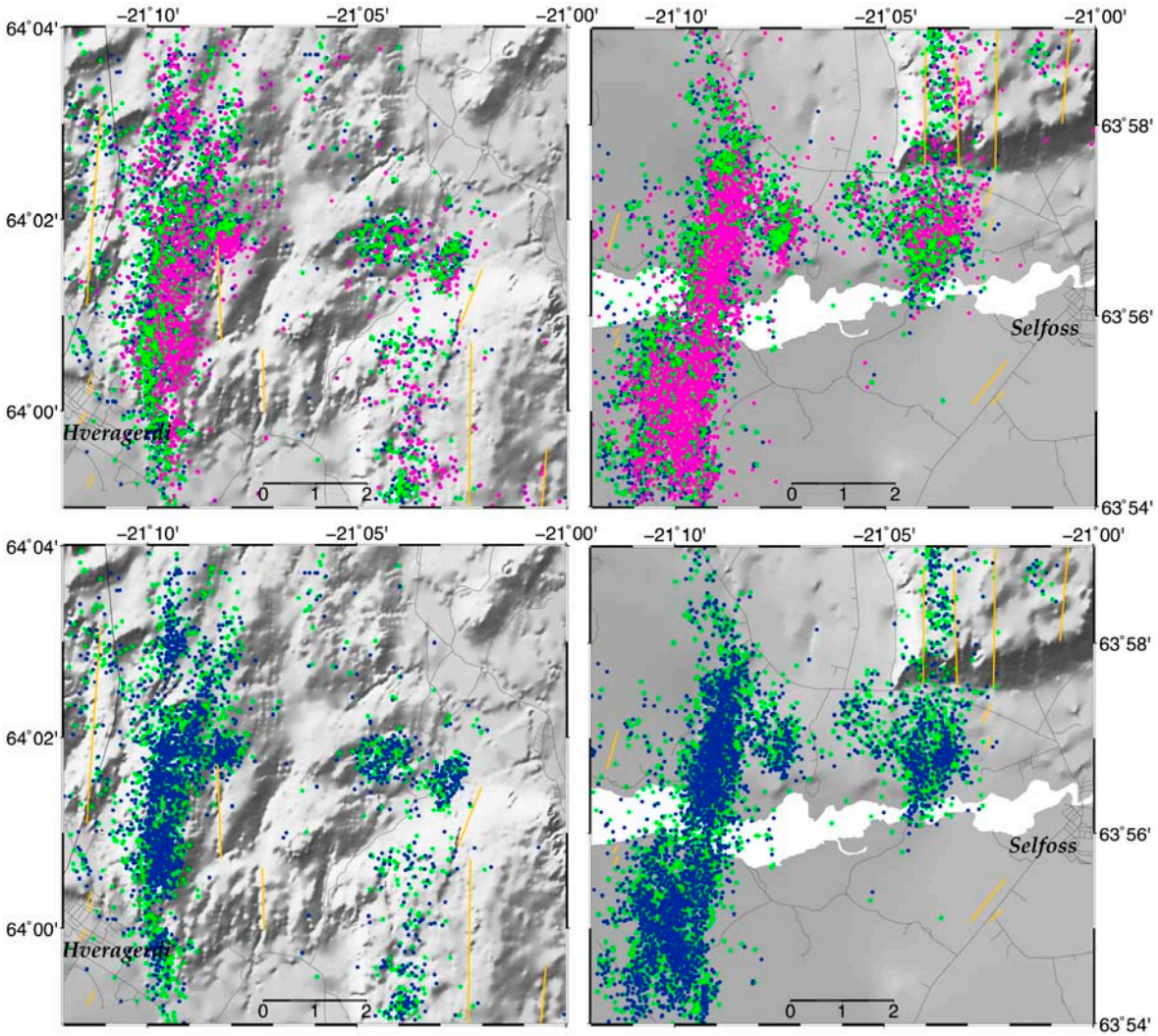

Figure 7. Top: A close up of the two main faults showing seismicity located by the SIL network (purple dots) on top of CMM locations using the same crustal model. Only events with epicentral location errors less than 1 km are shown. Below: A comparison of CMM locations with 14 stations using the SUL (green dots) and SIL (blue dots) models (Figure 8). Yellow lines mark mapped surface faults (Einarsson, this issue). – *Upptakasvæði eftirskjálfta við Hveragerði (Reykjafjall eða Kross misgengið) og Ingólfsfjall. Efri myndin sýnir samanburð á CMM og SIL staðsetningum með sama hraðalíkani (SIL). Neðri myndin sýnir samanburð á CMM staðsetningum með hraðalíkönunum SUL (grænir hringir) og SIL (dökkbláir hringir). Hraðalíkönin má sjá á 8. mynd. Kortlagðar sprungur á yfirborði eru gular, sjá grein Páls Einarssonar í þessu hefti.*

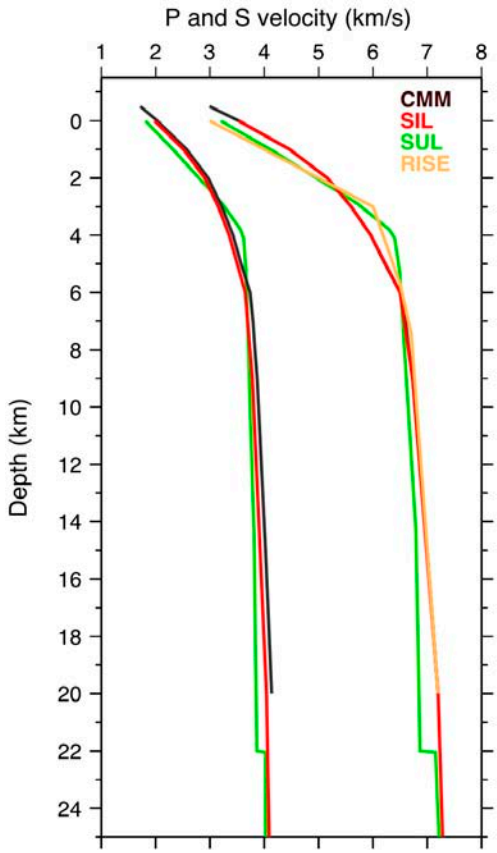

Figure 8. One-dimensional velocity models used for CMM locations. The SIL model is derived from the SIST refraction profile (Bjarnason *et al.*, 1991). The SUL model is derived from crustal profiling using relatively located earthquakes in the Hengill region (Vogfjörd *et al.*, 2002). The RISE model is derived from the RISE seismic refraction profile (Weir *et al.*, 2001). Depth datum is sea level. – *Hraðalíkön af Hengilssvæði og Suðurlandi unnin úr bylgjubrotsmælingum og afstæðum skjálftastaðsetningum. Við CMM staðsetningar er notað sama hraðalíkan og SIL netið notar. Staðsetningar með RISE og SUL hraðalíkönunum voru reiknaðar til samanburðar.*

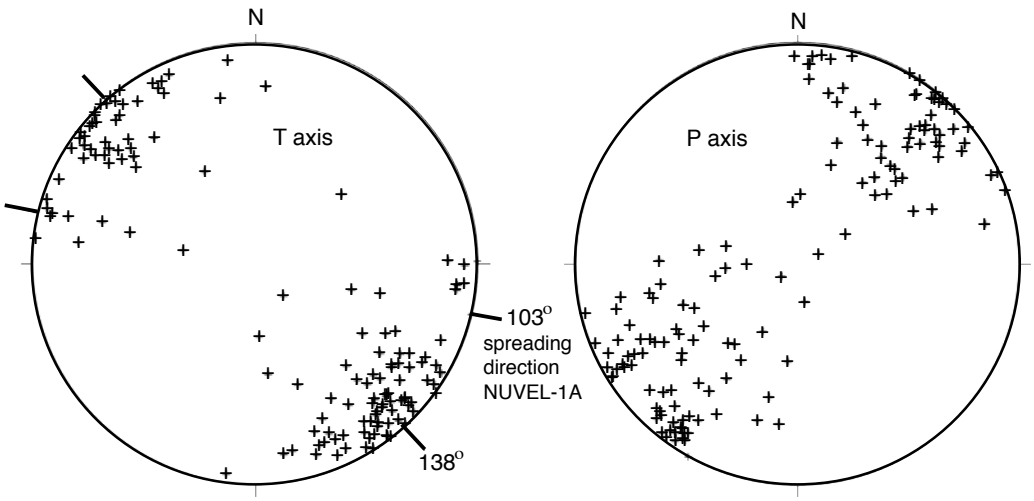

Figure 9. Lower hemisphere equal area projections of T and P axes from fault plane solutions. The overall spreading direction from NUVEL-1A is also shown. – *Brotlausnir sýna að stefna mestu togspennu (T) er 138°, þvert á rekbeltin.*

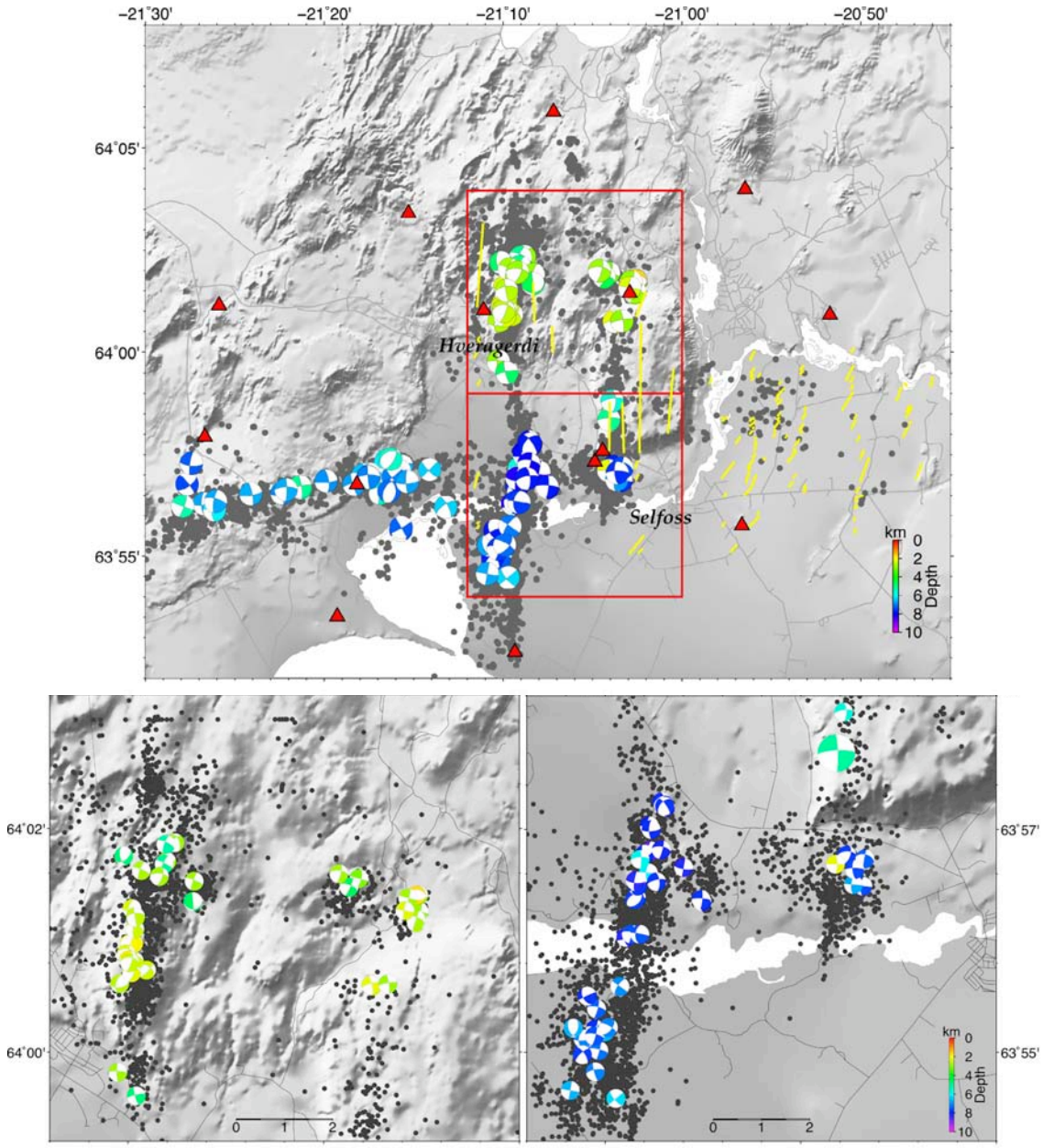

Figure 10. Map of fault plane solutions, color coded by depth. Note the systematic alignment of the strike-slip focal planes within the aftershock zone (grey dots) suggesting a right-lateral sense of motion on most of the fault strands. Red boxes mark sections of the main faults shown below. An enlarged fault plane solution from the initial event is shown on the lower right image. Red triangles denote seismic stations. – *Brotlausnir 123 skjálfta með auðlesnar P-bylgjur á 14 mælistöðvum (rauðir þríhyrningar), litaðar eftir dýpi. Upptakahreyfingar flestra skjálftanna gefa til kynna hægri-handar sniðgengi á N-S lægum misgengjum. Nokkrar brotlausnir sýna gliðnun (siggengi) á afmörkuðu svæði við Hjalla í Ölfusi og norðan Hveragerðis.*

components, in addition to a few purely normal events with similar N5–15°E strike. A majority of the focal mechanisms and distribution of aftershocks thus indicate N-S aligned right lateral movement along the two major fault zones, although focal solutions along the E-W oriented epicentral zone further west may be indicative of strike-slip motion on both N-S and E-W oriented faults.

A lower hemisphere equal area projection of the T axes (Figure 9) shows a strong horizontal NW-SE alignment (130°–140°), with an average of 138°. Similarly, plots of the P axes show a NE-SW trend of steeply dipping as well as horizontal axes associated with normal and strike-slip events, respectively. These directions are consistent with both strike-slip and normal earthquakes being generated by oblique movement with respect to the 103° spreading direction from NUVEL-1A (DeMets *et al.*, 1994). The NW-SE direction is close to being perpendicular to volcanic fissure swarms within the Reykjanes Peninsula Rift Zone and Western Volcanic Zone (Clifton and Kattenhorn, 2006). Mapping of Holocene surface faults within the SISZ (Einarsson, this issue) shows individual N-N20E aligned fault systems to be made up of a series of NE *en echelon* fault strands (Figures 1 and 5) indicative of variable obliquity of the bookshelf faulting along the SISZ.

DISCUSSION

Aftershock occurrence frequency

A histogram of earthquake occurrence in one hour bins (Figure 11) shows aftershock frequency decay, interrupted by an increase in seismicity May 31–June 1, June 2–4, 6–7 and 8–9. Although wind records from local weather stations (Ingólfsfjall and Eyrarbakki) reveal a clear inverse correlation between the number of earthquakes recorded and wind strength the increase in seismicity in early June is also observed in the number of CMM located events with higher signal-to-noise ratio as well as the number of events $M_{lw} \geq 3$ located by the SIL network (Figure 2 and black stars in Figure 11). The earthquake activity thus deviates from the empirical Omori's Law, which states that aftershock activity should decay exponentially with time (Utsu, 1965).

A fault reaches steady state over time, when slip rate has decreased to the tectonic loading rate. As the aftershock rate does not simply scale with stress rate, reloading of faults by afterslip can trigger aftershocks over various time periods, thus adding complexity to the rate-and-state dependent friction law and making it difficult to infer the mechanisms responsible for earthquake triggering on the basis of observations of stress changes (Helmstetter and Shaw, 2009). Although it is likely that the Reykjafjall event, which occurred within 3s of the Ingólfsfjall event (Decriem *et al.*, 2010), was generated by near-field dynamic triggering as during the June 2000 events (Antonioli *et al.*, 2006), faults within the SISZ and RPRZ are subjected to both dynamic and static triggering (Árnadóttir *et al.*, 2004). An increase in aftershock seismicity on May 31–June 1, June 2–4, 6–7 and 8–9 is thus most likely caused by short-term static stress buildup on adjacent faults due to abrupt changes in upper crustal pore pressure. A relatively fast viscoelastic response of the lower crust may also play a role. Pore-pressure oscillations can affect two-phase flow within geothermal areas. Some of the triggered seismicity originated within geothermal areas north of Hveragerði (Grensdalur) and at the junction of the SISZ with the southern Hengill Rift Zone.

A clear cyclicity in the number of aftershocks with a 24 hour periodicity is obvious in the CMM located events. No tidal forcing effect is observed. In order to establish the exact period of the cycle a Fourier Transform of the histogram was produced showing a peak of 1.001 days which means that the cycle of increase and decrease in aftershock frequency is, to within a minute or so, precisely one day. The wind records show the wind force being generally lower during the night hours. The permanent stations used by SIL are buried in vaults and thus not as sensitive to wind and cultural noise as the surface installed temporary stations which were also located adjacent to some of the major roads in the region (Figure 5). The 24 hour cycle, with about ten times fewer events detected during the daytime, is most likely due to higher cultural background noise during the day, causing fewer events to be detected by the CMM program's threshold SNR value.

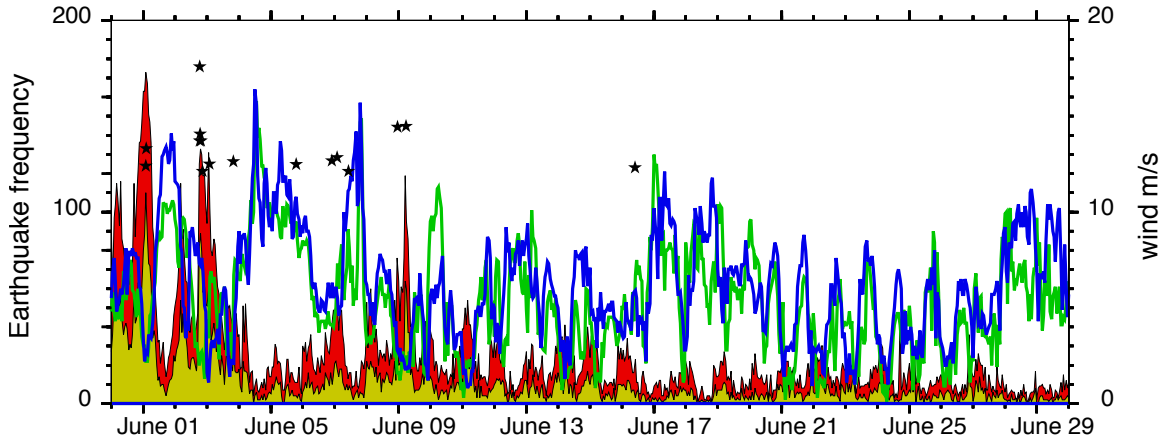

Figure 11. A histogram of aftershocks in one hour bins, from May 31th to June 29nd, using 19449 CMM locations (red bars). Note the strong 24 hour periodicity as well as enhanced activity May 31–June 1, June 2–4, June 6–7 and June 8–9. Filtered CMM locations (8233 events, yellow bars) show same trend. Blue and green graphs show wind strength at two weather stations within the epicentral region, Eyrarbakki (blue) and Ingólfsfjall (green). Black stars denote SIL located earthquakes M_{lw} 3 and larger (Figure 2). – *Fjöldi staðsettra skjálfta á hverri klukkustund (rauðar og gular súlur) ásamt vindhraða á sjálfvirkum veðurstöðvum við Eyrarbakka og Ingólfsfjall (bláar og grænar línur). Aukinn vindhraði minnkar næmni jarðskjálftamælanna. Svartar stjörnur sýna skjálfta M 3 og stærri skv. 2. mynd.*

Aftershock distribution

Close to 40 small foreshocks occurred within an hour prior to the main event at 1545h, on May 29th, the largest M_{lw}=3.5 at 1441h (Figure 2). Although the SIL catalogue of events is incomplete during Julian days 150–154, the cumulative strain release during aftershock activity of two similar sized main events seems to vary considerably between the two faults (Figure 12). Immediately following the main events, about 40 aftershocks M_{lw}=3–4.75 were located along the western (Reykjafjall) fault whereas only a few aftershocks of this magnitude were located along the eastern (Ingólfsfjall) fault. Triggered earthquake activity is also more pronounced westwards along the SISZ, with nearly twenty events M_{lw}> 2.5 originating along the E-W zone, west of the main faults versus five events M_{lw}> 2.5 on N-S faults, east of the Ingólfsfjall fault. The elevated triggering of earthquakes westwards is, however, somewhat unexpected as major seismic swarms occurred in this region in 1993–1998, culminating with a M_l∼5.1 event in November 1998 (Jakobsdóttir *et al.*, 2002; Jakobsdóttir, 2008).

Both main events occurred along previously mapped surface fault zones (Einarsson, this issue). Temporal and spatial aftershock patterns indicate that the two main fault zones are made up of many singular fault strands (Figures 5 and 10), concurrent with surface mapping of en echelon fault segments (Clifton and Einarsson, 2005). The epicentral zone of the western fault is divided into two main sections striking N10–15°E. Fault plane solutions obtained for 123 aftershocks greater than M_{lw}=1.3 are mostly strike-slip. However, a few normal faulting and dip-slip events occur at the junction of the western (Reykjafjall, Kross) fault with the E-W zone, north of Hveragerði and close to 63°N57.2' and 21°W17', just east of the SIL station Bjarnastaðir (BJA) (Figures 12–16) reflecting localized extension, down to about 9 km depth (Figure 5), i.e. the base of the seismogenic crust in this region (Stefánsson *et al.*, 1993). Both regions lie at the junction of the SISZ with volcanic rift zones of the Hengill and Grensdalur volcanic systems. Geothermal activity is also present.

Conjugate faulting is most pronounced northeast and southwest of the western fault (Figures 5 and 7), similar to conjugate faulting at the southern tip of the western SISZ2000 faults (Clifton and Einarsson, 2005; Hjaltadóttir and Vogfjörð, 2005). The northern, shallower ends of both 2000 faults ruptured a series of NNE-trending conjugate segments whereas similar SW striking forks are only observed along the southern, deeper, end of the western (Reykjafjall) fault (Figures 10 and 12–16). Scattered activity west and northwest of the northern end of the western fault may be related to short N-S or NW-SE striking fault strands. In spite of the two Ölfus events being of a smaller magnitude than the SISZ2000 main events, the aftershock zone of the 2008 events was of similar length and depth as the June 2000 faults. In particular, the 16.5 km long 2000 Hestvatn fault (Hjaltadóttir and Vogfjörð, 2005) is strikingly similar to the $\sim$17 km Reykjafjall fault, being divided into two sections, deepening southwards.

Frictional failure on critically stressed faults has been observed under the Coulomb failure criteria in geothermal and volcanic areas following large earthquakes (i.e. Peng *et al.*, 2010). The overall distribution of aftershocks along the main faults as well as triggered activity across the EW zone, coincides with the regions of highest Coulomb failure stress changes for two paired N-S right-lateral strike-slip faults (Decriem *et al.*, 2010). Aftershock activity following the M_w 6.5 June 2000 events also preferentially occurred in the dilatational (northeast and southwest) quadrants with postseismic deformation which extended about 5 km from the two main shock ruptures over a period of two months (Árnadóttir *et al.*, 2005). Whereas the short-term deformation has been explained by poroelastic rebound due to postearthquake pore pressure changes (Jónsson *et al.*, 2003) a year-scale deformation is explained by afterslip at 8–14 km depth or lower crustal viscoelastic relaxation (Árnadóttir *et al.*, 2005). Kinematic modelling based on geodetic measurements further suggest that the SISZ is a complex zone of N-S surface faulting driven by an E-W left-lateral shear below 15–20 km depth with a deep slip rate of 19 mm/yr (Árnadóttir *et al.*, 2006). The overall distribution of the 2008 aftershock zone and fault plane solutions are consistent with both strike-slip and normal earthquakes being generated by oblique movement with respect to the 103° spreading direction from NUVEL-1A concurrent with volcanic fissure swarms within the RPRZ and WVZ. Furthermore, triggered events west of the main faults, may indicate reloading by afterslip making it difficult to infer the mechanisms responsible for the earthquake triggering on the basis of short-term stress changes.

CONCLUSIONS

Using a new automated CMM technique a total of 19450 events, recorded on a 14-station network were located during the period May 30–July 2. Filtering based on SN ratios and location errors resulted in 7846 usable event locations.

Earthquake aftershocks delineate two major 12–17 km long, right lateral, strike slip faults, which rupture to greater depth (9 km) in the south than in the north (1–6 km). Most of the located events lie along the two main N-S faults, but the aftershock distribution reveals several smaller parallel faults as well as conjugate NE-SW and ENE-WSW oriented faults.

A comparison of CMM and SIL locations revealed a systematic westward shift of shallower events which we attribute to variation in station distribution and possible 3D variations in upper crustal structure.

The aftershock distribution along the two faults is indicative of the main fault movement having been in the centre of the fault, in agreement with the GPS modeling of Hreinsdóttir *et al.* (2009) and Decriem *et al.* (2010).

An increase in aftershock seismicity on May 31–June 1, June 2–4, 6–7 and 8–9 is most likely caused by short-term static stress buildup on adjacent faults. Short-term viscoelastic response of the lower crust may also be a contributing factor.

A third region of aftershocks marks a more complex area of activity to the west of the main faults. Some event distributions and fault plane solutions align to suggest slip on smaller NS faults in this region. However, left lateral strike slip features cannot be excluded in this zone, although probably with very limited slip.

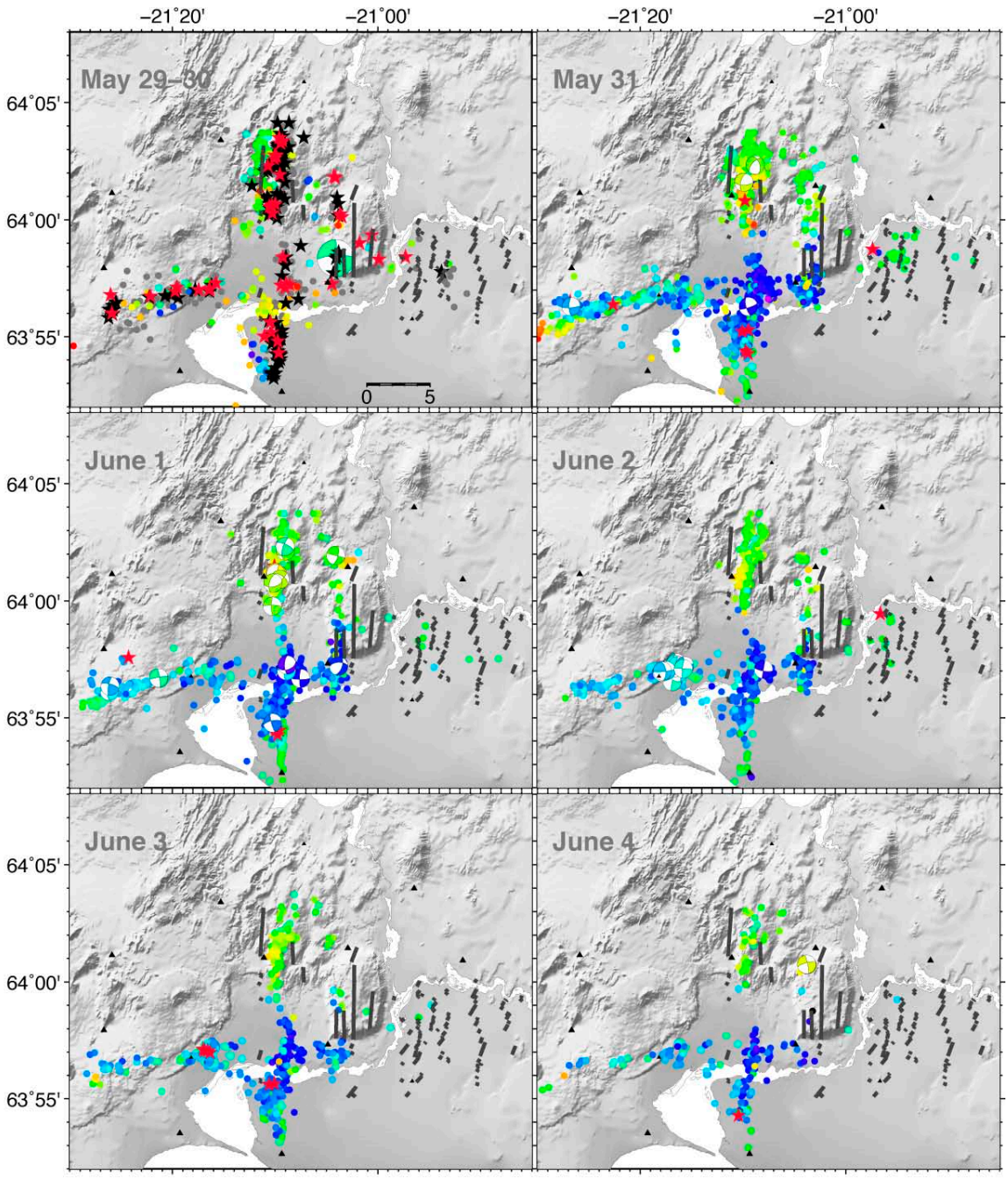

Figure 12. Daily activity May 29–June 4 and fault plane solutions based on CMM locations, colored by depth, see Figure 10. SIL located events $M_{lw} > 0.5$ on May 29 are grey whereas black stars denote $M_{lw} > 2.5$ events. $M_{lw} > 2.5$ events on other days are marked by red stars. – *Daglegur fjöldi staðsettra skjálfta ásamt brotlausnum, litaðir eftir dýpi. Stjörnur tákna skjálfta stærri en 3 stig. Svartir þríhyrningar tákna mælistöðvar.*

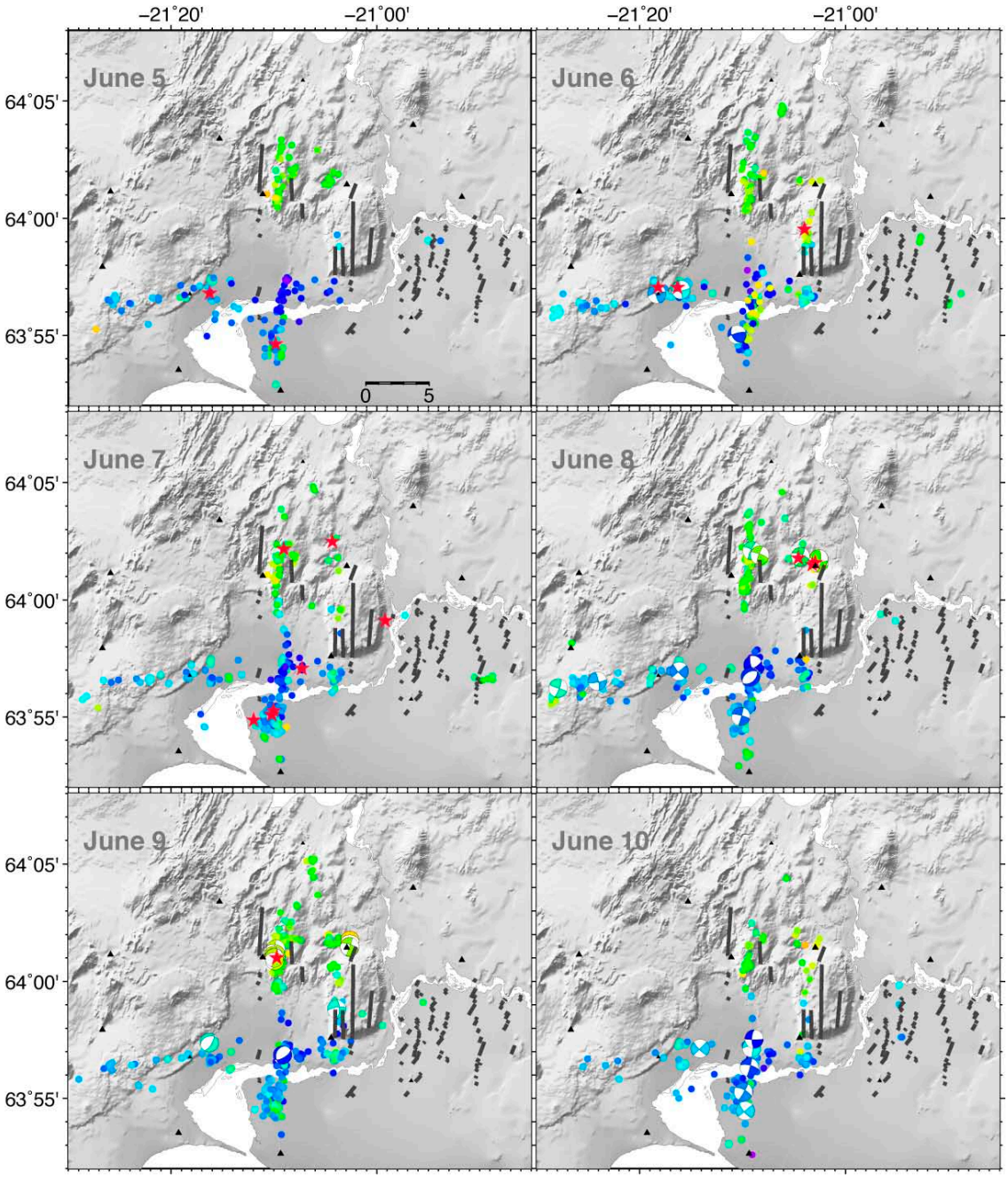

Figure 13. Daily activity June 5–10 with fault plane solutions based on CMM locations, colored by depth. – *Daglegur fjöldi staðsettra skjálfta 5.–10. júní ásamt brotlausnum, litaðir eftir dýpi.*

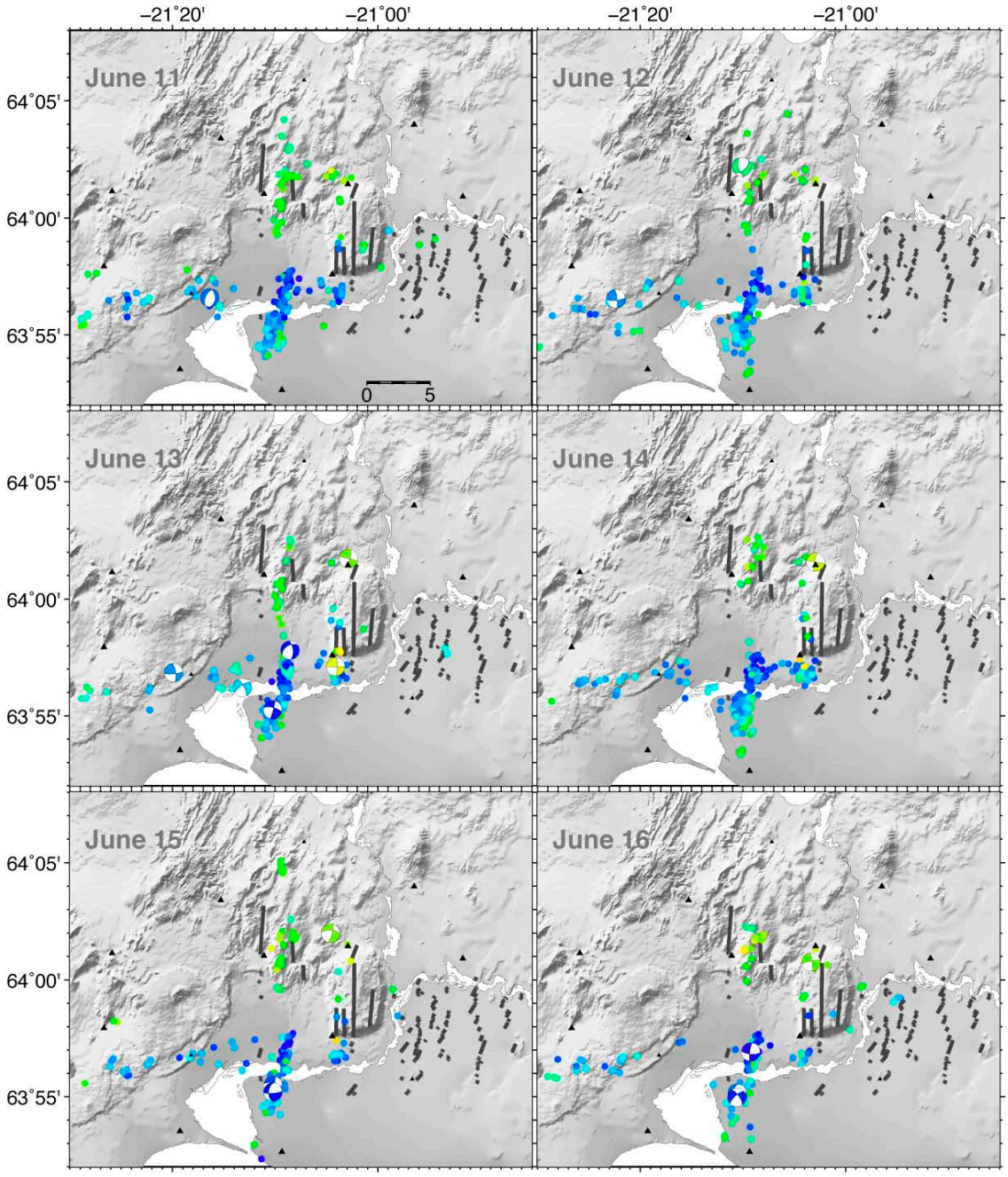

Figure 14. Daily activity June 11–16 with fault plane solutions, colored by depth. – *Daglegur fjöldi staðsettra skjálfta 11.–16. júní ásamt brotlausnum, litaðir eftir dýpi.*

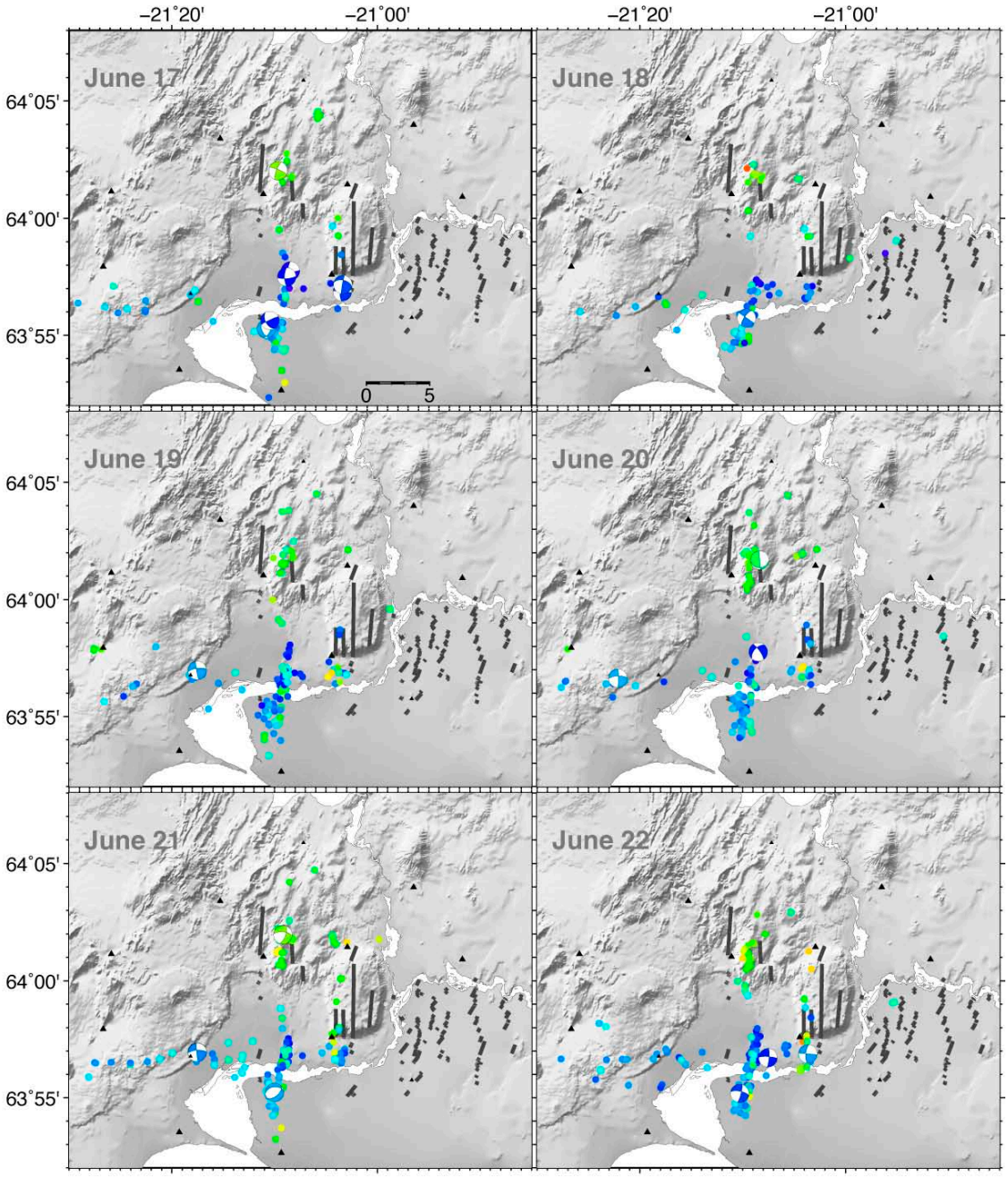

Figure 15. Daily activity June 17–22 with fault plane solutions, colored by depth. – *Daglegur fjöldi staðsettra skjálfta 17.–22. júní ásamt brotlausnum, litaðir eftir dýpi.*

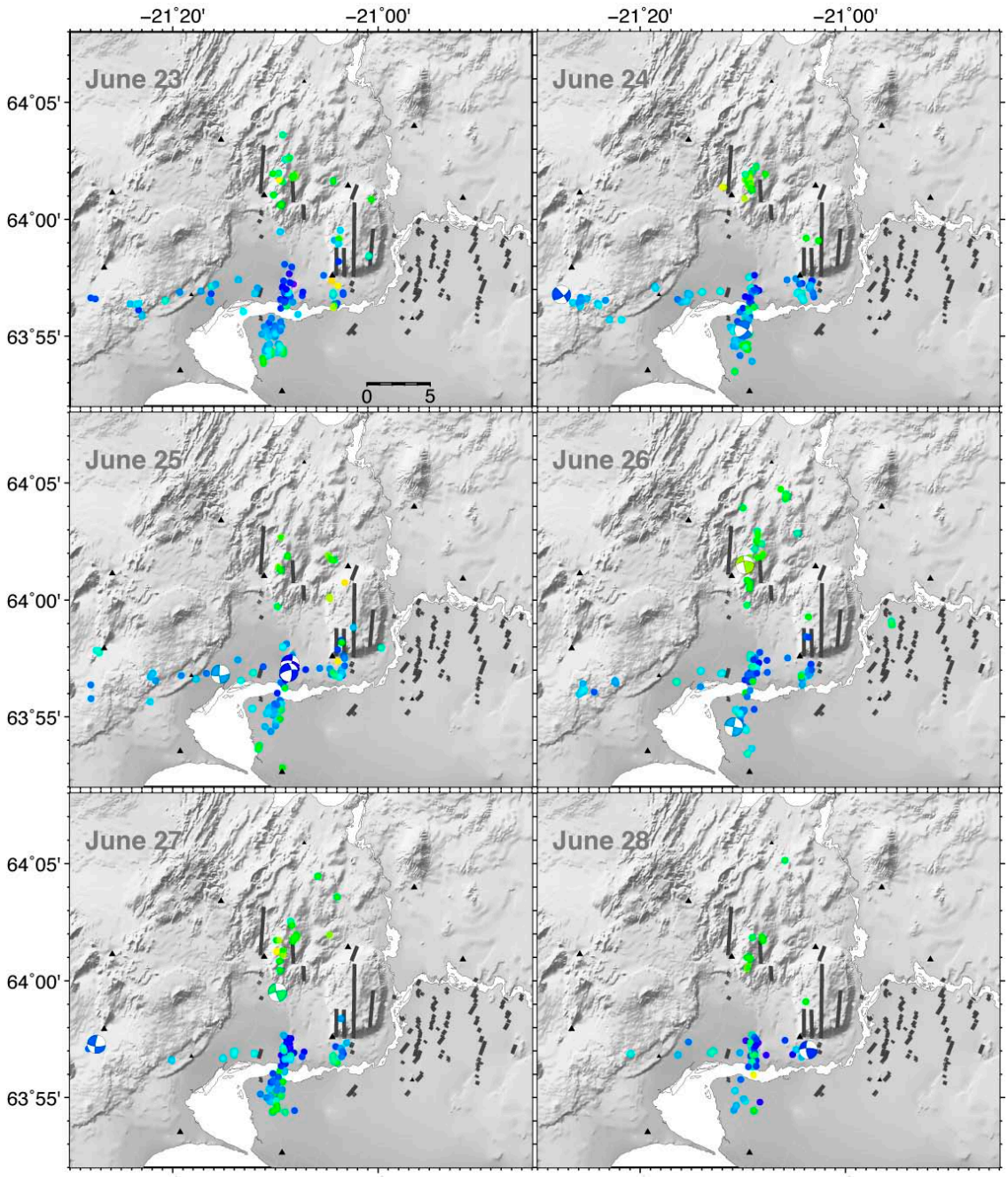

Figure 16. Daily activity June 23–28 with fault plane solutions, colored by depth. – *Daglegur fjöldi staðsettra skjálfta 23.–28. júní ásamt brotlausnum, litaðir eftir dýpi.*

Fault plane solutions are consistent with both strike-slip and normal earthquakes being generated by oblique movement with respect to the 103° spreading direction from NUVEL-1A but perpendicular to volcanic fissure swarms within the Reykjanes Peninsula Rift Zone and the Western Volcanic Zone.

Acknowledgements

Ingi Þ. Bjarnason, Birgit Ruff, Indíana Elín Ingólfsdóttir, Magnús Pálsson and Rögnvaldur Magnússon helped install and maintain the temporary SISZ2008 network. Janet Key and Nigel Woodcock provided helpful advice and Andrew Feldhaus helped with Fourier transforms in Matlab. Páll Einarsson made his surface fault location data available and Guðrún Gísladóttir, Icelandic Meteorological Office, provided wind recordings from automated weather stations within the survey region. Generic Mapping Tools (Wessel and Smith, 1991) were used to produce the figures. Reviews by Kristín Vogfjörð and an anonymous reviewer improved this paper.

ÁGRIP

Í kjölfar jarðskjálftanna við Ingólfsfjall og Hveragerði, þann 29. maí 2008 voru ellefu færanlegir jarðskjálftamælar settir upp á svæðinu. Nýtt forrit (CMM) var notað til að greina og staðsetja jarðskjálfta sem skráðir voru á færanlegu stöðvarnar sem og þrjár SIL-stöðvar (1., 3. og 4. mynd). Forritið staðsetti alls tæplega 20 þúsund skjálfta á tímabilinu 30. maí til 2. júlí, þar af voru 7846 jarðskjálftar með reiknaðri staðsetningaróvissu innan við 1 km í lárréttu plani og 2 km í dýpi. Flestir eftirskjálftanna liggja eftir vesturjaðri Ingólfsfjalls og Reykjafjalls (Kross) við Hveragerði (5. mynd), á upptakamisgengjum $M_w \geq 6$ skjálftanna. Eftirskjálftar við vesturjaðar Ingólfsfjalls spanna um 13 km NS, en vestara misgengið við Reykjafjall nær 17 km lengd. Flestir eftirskjálftanna raða sér norður og suður af upptökum meginskjálftanna. Einnig var töluverð virkni á AV belti vestur um Ölfusið. Upptakadýpi eykst til suðurs, frá 3–5 km til 8–9 km (6. mynd). Þéttara stöðvanet gefur aukna nákvæmni í dýptardreifingu skjálftanna (5., 6. og 7. mynd). CMM staðsettir skjálftar á minna en 3–4 km dýpi liggja allt að 500 m vestar en SIL staðsetningar með sama hraðalíkani (7. og 8. mynd). Hliðrunin er í samræmi við niðurstöður GPS-mælinga á svæðinu (Decriem og fl., 2010) sem og sprungumyndun á yfirborði, rétt vestan Ingólfsfjalls. CMM staðsetningarnar með þremur mismunandi hraðalíkönum af Suðurlandi gáfu ekki marktæk frávik. Brotlausnir 123 skjálfta gefa til kynna hægri-handar sniðgengishreyfingar á NS-lægum misgengjum (9. og 10. mynd) eftir vesturjaðri Ingólfsfjalls og Reykjafjalls (5. mynd). Ás mestu togspennu liggur nálægt 138 gráðum, þvert á sprungureinar Vestara gosbeltisins. Nokkrar brotlausnir hafa siggengisþátt sem bendir til gliðnunarhreyfinga samhliða sniðgengishreyfingunum. Flestar þeirra eru á afmörkuðu svæði við Hjalla í Ölfusi og norðan Hveragerðis. Jarðhitavirkni er á báðum þessum stöðum. Um 40 litlir forskjálftar mældust á SIL stöðvum Veðurstofunnar fyrir aðalskjálftann kl. 1645 þann 29. maí, sá stærsti M_{lw}=3.5 kl. 1441. Fjöldi eftirskjálfta er mestur fyrstu dagana en dvínar síðan hratt með tíma (2. og 11. mynd). Þar sem stöðvarnar voru settar út í flýti var frágangur þeirra ekki nægilega vandaður til þess að útiloka vindsuð og önnur umhverfisáhrif. Daglegur fjöldi staðsettra smáskjálfta endurspeglar því bæði skjálftavirknina sem og vindstyrk á svæðinu. Í kjölfar meginskjálftanna urðu tugir skjálfta M_{lw}3–4.75 á vestara misgenginu en einungis nokkrir á austara misgenginu og þar austuraf (12.–16. mynd). Þessi hegðun endurspeglar sögulega þróun landskjálfta á þessu svæði þar sem virknin hefur hlaupið til vesturs.

REFERENCES

Antonioli, A., M. E. Belardinelli, A. Bizzarri and K. S. Vogfjord 2006. Evidence of instantaneous dynamic triggering during the seismic sequence of year 2000 in south Iceland. *J. Geophys. Res.* 111, B03302, doi:-10.1029/2005JB003935.

Árnadóttir, Th., H. Geirsson and P. Einarsson 2004. Coseismic stress changes and crustal deformation on the Reykjanes Peninsula due to triggered earthquakes on June 17, 2000. *J. Geophys. Res.* 109, B09307, doi:10.1029/2004JB003130.

Árnadóttir, Th., S. Jónsson, F. F. Pollitz, W. Jiang and K. L. Feigl 2005. Postseismic deformation following the June 2000 earthquake sequence in the

south Iceland seismic zone. *J. Geophys. Res.* 110, doi:10.1029/2005JB003701.

Árnadóttir, Th., W. Jiang, K. L. Feigl, H. Geirsson and E. Sturkell 2006. Kinematic models of plate boundary deformation in southwest Iceland derived from GPS observations. *J. Geophys. Res.* 111, doi:10.1029/2005-JB003907.

Bergerat, F. and J. Angelier 2003. Mechanical behavior of the Árnes and Hestfjall Faults of the June 2000 earthquakes in Southern Iceland: inferences from surface traces and tectonic model. *J. Struct. Geol.* 25, 1507–1523.

Bjarnason, I. Th. and P. Einarsson 1991. Source mechanism of the 1987 Vatnafjöll earthquake in South Iceland. *J. Geophys. Res.* 96, 4313–4324, doi:10.1029/-96GL00420.

Bjarnason, I. Th., P. A. Cowie, M. H. Anders, N. Seeber and C. H. Scholz 1993. The 1912 Iceland earthquake rupture: growth and development of a nascent transform system. *Bull. Seismol. Soc. Am.* 83, 416–435.

Bjarnason, I. Th., W. Menke, Ó.G. Flóvenz and D. Caress 1993. Tomographic image of the Mid-Atlantic plate boundary in southwestern Iceland. *J. Geophys. Res.* 98, 6607–6622.

Clifton, A. E. and S. A. Kattenhorn 2006. Structural architecture of a highly oblique divergent plate boundary segment. *Tectonophysics* 419, 27–40.

Clifton, A. E. and P. Einarsson 2005. Styles of surface rupture accompanying the June 17 and 21, 2000 earthquakes in the South Iceland Seismic Zone. *Tectonophysics* 396, 141–159.

CMT catalogue from the global CMT project. December 2009. http://www.globalcmt.org/CMTsearch.html.

Decriem, J., T. Árnadóttir, A. Hooper, H. Geirsson, F. Sigmundsson, M. Keiding, B. G. Ófeigsson, S. Hreinsdóttir, P. Einarsson, P. LaFemina and R. A. Bennett 2010. The 2008 May 29 earthquake doublet in SW Iceland. *Geophys. J. Int.* 181, 1128–1146, doi:-10.1111/j.1365-246X.2010.04565.x

DeMets, C., R. G. Gordon, D. F. Argus and S. Stein 1994. Effect of recent revisions to the geomagnetic reversal time scale on estimates of current plate motions. *Geophys. Res. Lett.* 21, 2191–2194.

Drew, J., D. Leslie, P. Armstrong and G. Michaud 2005. Automated microseismic event detection and location by continuous spatial mapping. Abstract SPE 95513 in: *Proceedings, Soc. Petroleum Engineers.* Annual Technical Conference and Exhibition, 733–739.

Drew, J., D. 2010. *Coalescence microseismic mapping: an imaging method for the detection and location of seismic events.* PhD dissertation, University of Cambridge.

Dubois L., K. L. Feigl, D. Komatitsch, Th. Arnadottir and F. Sigmundsson 2008. Three-dimensional mechanical models for the June 2000 earthquake sequence in the south Iceland seismic zone. *Tectonophysics* 457, 12–29, doi: 10.1016/j.tecto.2008.05.020.

Duyster, J. 2000. *StereoNett*, version 2.46. http://www.-ruhr-uni-bochum.de/hardrock/downloads.htm.

Einarsson, P. 1991. Earthquakes and present-day tectonism in Iceland. *Tectonophysics* 189, 261–279.

Einarsson, P. 2010. Mapping of Holocene surface ruptures in the South Iceland Seismic Zone. *Jökull* 60, 117–134.

Einarsson, P. and S. Björnsson 1979. Earthquakes in Iceland. (Jarðskjálftar á Íslandi). *Jökull* 29, 37–43.

Einarsson, P., S. Björnsson, G. Foulger, R. Stefánsson and Þ. Skaftadóttir 1981. Seismicity pattern in the South Iceland seismic zone. In: Simpson, D. and P. Richards (eds.). *Earthquake Prediction–An International Review.* Am. Geophys. Union, Maurice Ewing Series 4, 141–151.

Einarsson, P. and J. Eiríksson 1982. Earthquake fractures in the districts Land and Rangárvellir in the South Iceland Seismic Zone. *Jökull* 32, 113–120.

Einarsson, P. and K. Saemundsson 1987. Earthquake epicenters 1982–1985 and volcanic systems in Iceland (map). In: Sigfússon, Th. (ed.), *Í hlutarins eðli: Festschrift for Thorbjorn Sigurgeirsson.* Menningarsjóður, Reykjavík.

Hackman, M., G. King and R. Bilham 1990. The mechanics of the South Iceland Seismic Zone. *J. Geophys. Res.* 95, 17.339–17.351.

Halldórsson B. and R. Sigbjörnsson 2009. The M_w 6.3 Ölfus earthquake at 15:45 UTC on 29 May 2008 in South Iceland: ICEARRAY strong-motion recordings. *Soil Dynamics and Earthquake Engineering* 29, 1073–1083. doi:10.1016/j.soildyn.2008.12.006.

Helmstetter A., and B. E. Shaw 2009. Afterslip and aftershocks in the rate-and-state friction law. *J. Geophys. Res.* 114, B01308, doi:10.1029/2007JB005077.

Hjaltadóttir, S. and K. S. Vogfjörð 2005. *Subsurface fault mapping in Southwest Iceland by relative location of aftershocks of the June 2000 earthquakes.* Report VÍ-ES-01, 18 pp.

Hreinsdóttir, S., P. Einarsson and F. Sigmundsson 2001. Crustal deformation at the oblique spreading Reykjanes Peninsula, SW Iceland: GPS measurements from 1993 to 1998. *J. Geophys. Res.* 106, 13,803–13,816.

Hreinsdóttir, S., T. Árnadóttir, J. Decriem, H. Geirsson, A. Tryggvason, R. A. Bennett and P. LaFemina 2009. A complex earthquake sequence captured by the continuous GPS network in SW Iceland. *Geophys. Res. Lett.* 36, L12309, doi:10.1029/2009GL038391.

Jakobsdóttir, S. S., G. B. Guðmundsson and R. Stefánsson 2002. Seismicity in Iceland 1991– 2000 monitored by the SIL system. *Jökull* 52, 87–94.

Jakobsdóttir, S. S. 2008. Seismicity in Iceland: 1994–2007. *Jökull* 58, 75–100.

Jónsson, S., P. Segall, R. Pedersen and G. Björnsson 2003. Post-earthquake ground movements correlated to pore-pressure transients. *Nature* 424, 179–183.

Pedersen, R., S. Jónsson, T. Árnadóttir, F. Sigmundsson and K. L. Feigl 2003. Fault slip distribution of two M_w=6.5 earthquakes in South Iceland estimated from joint inversion of InSAR and GPS measurements. *Earth Planet. Sci. Lett.* 213, 487–502.

Peng, Z., D. P. Hill, D. R. Shelly and C. Aiken 2010. Remotely triggered microearthquakes and tremor in central California following the 2010 M_w 8.8 Chile earthquake, *Geophys. Res. Lett.* 37, L24312, doi:10.1029/-2010GL045462.

Reasenberg, P. A. and D. Oppenheimer 1985. *FPFIT, FPPLOT and FPPAGE: Fortran computer programs for calculating and displaying earthquake fault-plane solutions.* US Geological Survey Open-File report, 85–739.

Richards-Dinger, K. B. and P. M. Shearer 2000. Earthquake locations in southern California obtained using source-specific station terms. *J. Geophys. Res.* 105, 10,939–10,960, doi:10.1029/2000JB900014

Rognvaldsson, S. Th. and R. Slunga 1994. Single and joint fault plane solutions for microearthquakes in South Iceland. *Tectonophysics* 237, 73–86, doi:10.1016/-0040-1951(94)90159-7.

Saemundsson, K. 1995. *Svartsengi geological map (bedrock)* 1:25000. Orkustofnun, Hitaveita Sudurnesja and Landmaelingar Islands. Reykjavik.

Saemundsson, K. and S. Einarsson 1980. *Geological map of Iceland, sheet 3, SW-Iceland, second ed.*. Museum of Natural History and the Iceland Geodetic Survey, Reykjavik.

Sigmundsson, F., P. Einarsson, R. Bilham and E. Sturkell 1995. Rift-transform kinematics in south Iceland: deformation from global positioning system measurements, 1986 to 1992. *J. Geophys. Res.* 100, 6235–6248.

Sigmundsson, F., P. Einarsson, S. Rögnvaldsson, G. Foulger, K. Hodgkinson and G. Thorbergsson 1997. The 1994–1995 seismicity and deformation at the Hengill triple junction, Iceland: Triggering of earthquakes by minor magma injection in a zone of horizontal shear stress. *J. Geophys. Res.* 102, 15151–15161.

SIL preliminary earthquake event database from the Iceland Meteorological Office November 2009. http://-hraun.vedur.is/ja/englishweb/uppl_gagnag_ensk.html

Stefánsson, R., R. Böðvarsson, R. Slunga, P. Einarsson, S. Jakobsdóttir, H. Bungum, S. Gregersen, J. Havskov, J. Hjelme and H. Korhonen 1993. Earthquake prediction research in the South Iceland Seismic Zone and the SIL project. *Bull. Seismol. Soc. Am.* 83, 696–716.

Tarantola, A. and B. Valette 1982. Inverse Problems - Quest for Information. *J. Geophys.* 50, 159–170.

Utsu, T. 1965. Aftershocks and earthquake statistics. *J. Fac. Sci. Hokkaido University* VII, 379–441.

Vogfjörd, K. S., G. Nolet, W. J. Morgan, R. M. Allen, R. Slunga, B. H. Bergsson, P. Erlendsson, G. Foulger, S. Jakobsdottir, B. Julian, M. Pritchard and S. Ragnarsson 2002. Crustal profiling in Iceland using earthquake source arrays. *Eos Trans. AGU*. S61C-1161.

Vogfjörd, K. S., S. Hjaltadóttir and R. Slunga 2005. Volcano tectonic interaction in the Hengill region, Iceland during 1993–1998. *Geophys. Res. Abstracts*, 7, EUG2005-09947.

Waldhauser, F. and W. Ellsworth 2000. A double-difference earthquake location algorithm; method and application to the northern Hayward Fault, California. *Bull. Seismol. Soc. Am.* 90, 1353–1368.

Weir, N. R., R. S. White, B. Brandsdóttir, P. Einarsson, H. Shimamura, H. Shiobara and the RISE fieldwork team 2001. Crustal structure of the Northern Reykjanes Ridge and Reykjanes Peninsula, South-west Iceland. *J. Geophys. Res.* 106, 6347–6368.

Wessel, P. and W. H. F. Smith 1991. Free software helps map and display data. *Eos, Trans. AGU* 72, 41.